AIAA JOURNAL
Vol. 31, No. 12, December 1993

Analysis of Thermochemical Nonequilibrium Models for Carbon Dioxide Flows

Stacey G. Rock*
Center for Space Transportation and Applied Research, Tullahoma, Tennessee 37388
Graham V. Candler†
University of Minnesota, Minneapolis, Minnesota 55455
and
Hans G. Hornung‡
California Institute of Technology, Pasadena, California 91125

The aerothermodynamics of thermochemical nonequilibrium carbon dioxide flows are studied. The chemical kinetics models of McKenzie and Park are implemented in a three-dimensional computational fluid dynamics code. The code incorporates a five-species gas model characterized by translational-rotational and vibrational temperatures. Solutions are obtained for flow over finite-length elliptical and circular cylinders for a freestream condition of $u_\infty = 4.24$ km/s, $T_\infty = 1970$ K, and $h_{0\infty} = 9.0$ MJ/kg. The computed flowfields are then employed to calculate Mach-Zehnder interferograms for comparison with experimental data. The accuracy of the chemical kinetics models is determined through this comparison. Also, the methodology of the three-dimensional thermochemical nonequilibrium code is verified by the reproduction of the experiments.

Introduction

THE accurate modeling of reacting carbon dioxide flows is of importance in Martian atmospheric entry, where the atmosphere is composed primarily of CO_2. Hypersonic flows over vehicles with carbon-based ablators is another area where the chemical kinetics of carbon dioxide become important. The type of chemical kinetics model used directly affects the aerodynamic and heating characteristics of these vehicles. For this and other reasons, there is interest in determining which of the current chemical kinetics models is most accurate.

The two primary chemical kinetics models in use are the ones developed by McKenzie[1] and by Park et al.[4] The first model was developed by McKenzie[1] in the mid 1960s, and was extended in the work of Evans et al.[2] and Grose et al.[3] who studied the effects of nonequilibrium chemistry on the Viking and Pioneer planetary entry probes. The second model was developed more recently by Park et al.[4] These models have been implemented in computational fluid dynamics codes to study Martian atmospheric entry. Candler[5] demonstrated that certain aspects of the flow solutions produced by the McKenzie model, primarily shock stand-off distance, compared well to experiment. Chen et al.[6] have used both the McKenzie and Park models to predict surface heating rates over Martian entry vehicles. Their findings indicate a significant difference between the heating rates predicted by the two models. However, the shock stand-off distance and shock shape predicted by the two models were similar. Therefore, a more detailed analysis is required to determine which of the models is more accurate, and whether the more accurate model can be further improved.

The detailed analysis of both chemical kinetics models is the purpose of this study. The reaction rate model and vibrational relaxation rate model are tested by comparison to experimental data obtained by Hornung. The data consist of a series of interferograms of dissociating CO_2 flows about circular and elliptical cylinders. The tests were conducted in 1971 in a large free piston shock tunnel, known as T3, located at the Australian National University. The series of Mach-Zehnder interferograms form a very valuable and reliable data base for validating current aerothermodynamic models for reacting CO_2 flows. Also, as compared to air or nitrogen, CO_2 is a gas in which the vibrational component of the energy is an order of magnitude more important in relation to the amount of energy absorbed by the dissociative reactions in the flow. Experiments in CO_2 are therefore a much more sensitive instrument for testing different chemistry and vibration models through experimental comparison to computational fluid dynamics (CFD). By computationally reproducing the interference patterns, the accuracy of current models can be investigated.

Thermophysical Model

The thermophysical model for a reacting CO_2 flow must allow for the presence of chemical and thermal nonequilibrium. Chemical nonequilibrium is accounted for by modeling the dissociating CO_2 flow as a mixture of chemically reacting species. For flows not involving ionization, such as those considered here, there are five primary chemical species, CO_2, CO, O_2, C, and O. The interaction of these species is governed by the chemical kinetics models of McKenzie or Park et al. The adaptation of these models into a CFD code capable of simulating chemical nonequilibrium flows is discussed in this section.

Vibrational Energy Model

Thermal nonequilibrium is accounted for by allowing the translational-rotational and vibrational energies to evolve at different rates. With the current model, the translational and rotational energy modes are assumed to be in equilibrium with each other at the translational-rotational temperature T. It is assumed that a separate vibrational temperature T_v characterizes the vibrational energy of all of the vibrational energy modes of the gas. This assumption requires that the vibrational modes are strongly coupled with one another so that they relax at the same rate. Camac[7] demonstrates that the three vibrational modes of CO_2 relax at the same rate. This

Presented as Paper 92-2852 at the AIAA 27th Thermophysics Conference, Nashville, TN, July 6–8, 1992; received Oct. 15, 1992; revision received May 17, 1993; accepted for publication May 19, 1993.

*Research Engineer. Member AIAA.
†Assistant Professor, Department of Aerospace Engineering and Mechanics. Member AIAA.
‡Director, Graduate Aeronautical Laboratories and Clarence L. Johnson Professor of Aeronautics. Member AIAA.

equilibration is due to strong resonance coupling between the different vibrational modes of CO_2.

The total vibrational energy of the CO_2 mixture is the sum of the individual vibrational energies of the molecular species. A simple harmonic oscillator is employed to describe the vibrational potential of each vibrational mode of the molecules. Carbon dioxide has three vibrational modes, one of which is doubly degenerate. With the assumption that there is a unique vibrational temperature at each point in the flowfield, the vibrational energy per unit mass of CO_2 is given by

$$e_{vCO_2} = e_{vCO_2,1} + e_{vCO_2,2} + e_{vCO_2,3} \tag{1}$$

where

$$e_{vCO_2,r} = g_r \frac{R}{M_{CO_2}} \frac{\theta_{vCO_2,r}}{e^{\theta_{vCO_2,r}/T_v} - 1} \tag{2}$$

where $\theta_{vCO_2,r}$ is the characteristic temperature of vibrational mode r, g_r is the degeneracy of that mode, R is the universal gas constant, and M_{CO_2} the atomic weight. The vibrational energy per unit mass of a diatomic species (CO, O_2) is given by

$$e_{vs} = \frac{R}{M_s} \frac{\theta_{vs}}{e^{\theta_{vs}/T_v} - 1} \tag{3}$$

where s represents either diatomic species. See Table 1 for the values of θ_{vs} and g_r.

The rate at which these vibrational energies relax toward the translational energy is assumed to behave according to the Landau-Teller relaxation expression[8]

$$Q_{vs} = \rho_s \frac{e_{vs}^*(T) - e_{vs}}{\tau_s} \tag{4}$$

where Q_{vs} is the rate of energy transfer to species s per unit volume, the term τ_s is the vibrational relaxation time, and $e_{vs}^*(T)$ is the vibrational energy evaluated at the local translational temperature T.

The relaxation time of species s due to collisions with species r, τ_{sr} is determined from an expression due to Millikan and White[9]

$$\ln \tau_{sr} p = 0.00116 \mu_{sr}^{1/2} \theta_{vs}^{4/3} (T^{-1/3} - \mu_{sr}^{1/4}) - 18.42 \tag{5}$$

where μ_{sr} is the reduced mass, p is the pressure in atmospheres, and τ_{sr} is in seconds. The relaxation time of species s is then the number-weighted average of τ_{sr}

$$\tau_s = \frac{\sum_r N_r}{\sum_r N_r / \tau_{sr}} \tag{6}$$

where N_r is the number density of species r. The Millikan-White formulation is in good agreement with experimental data for the diatomic species.[9,10] The Millikan-White expression for CO_2 predicts that the three vibrational modes of CO_2 will relax at different rates. The results of Camac[7] indicate that the three modes relax at the same rate, and the vibrational relaxation time of CO_2 can be modeled by

$$\ln \tau_{CO_2} p = 36.5 T^{-1/3} - 17.71 \tag{7}$$

where τ_{CO_2} is in seconds and p is in atmospheres. This relaxation time is similar to the one predicted by Millikan and White for the $\theta_v = 945$ K bending mode.[5] Therefore, the Millikan-White expression is in good agreement with the Camac expression if all of the modes are assumed to relax according to the $\theta_v = 945$ K bending mode. The expression developed by Camac is a fit to experimental data for $2000 < T < 6000$ K. This is the same temperature range being investigated in this study. Because of the temperature being relatively low and coinciding with the Camac data, the collision-limited value of the vibrational relaxation time τ_c proposed by Park[11] is not required. Both the Camac expression and the Millikan-White expression, modified using $\theta_v = 945$ K for all modes, are investigated in this study.

Chemical Kinetics Model

The chemical reactions considered for this flow are

$$\begin{aligned}
&1)\ CO_2 + M_1 \rightleftharpoons CO + O + M_1 \\
&2)\ CO + M_2 \rightleftharpoons C + O + M_2 \\
&3)\ O_2 + M_3 \rightleftharpoons O + O + M_3 \\
&4)\ CO_2 + O \rightleftharpoons O_2 + CO \\
&5)\ CO + O \rightleftharpoons O_2 + C \\
&6)\ CO + CO \rightleftharpoons CO_2 + C
\end{aligned} \tag{8}$$

where M represents any species that acts as a collision partner for the reaction. The six available reactions are governed by forward and backward reaction rate coefficients k_f and k_b, which have the Arrhenius form

$$\begin{aligned}
k_f &= C_f T^{\eta_f} \exp(-\theta_f/T) \\
k_b &= C_b T^{\eta_b} \exp(-\theta_b/T)
\end{aligned} \tag{9}$$

Table 1 Vibrational energy constants

Species	θ_v, K	g
CO_2	1903	1
	945	2
	3329	1
CO	3074	—
O_2	2239	—

Table 2 McKenzie reaction rate coefficients, $m^3/kmol \cdot s$ or $m^6/kmol^2 \cdot s$

Reaction no.	C_f	η_f	θ_d	C_b	η_b	θ_b
1	1.20×10^8	0.5	34,340	2.00×10^0	1.25	−28,400
2	4.48×10^{16}	−1.0	128,900	1.00×10^{12}	−1.0	0
3	9.05×10^{15}	−1.0	59,370	9.00×10^9	−0.5	0
4	2.54×10^8	0.5	27,690	5.00×10^5	1.0	23,900
5	2.73×10^9	0.5	69,540	9.40×10^9	0.25	0
6	2.33×10^6	0.5	65,710	4.60×10^9	−0.25	0

Table 3a Park et al. reaction rate coefficients, $m^3/kmol \cdot s$ or $m^6/kmol^2 \cdot s$

Reaction no.	C_f	η_f	θ_d	C_b	η_b	θ_b
1	3.70×10^{11}	0.0	52,500	6.10×10^3	0.75	−10,240
2	2.30×10^{16}	−1.0	129,000	5.13×10^{11}	−1.0	0
3	2.00×10^{18}	−1.5	59,500	2.00×10^{12}	−1.0	0
4	1.70×10^{10}	0.0	26,500	3.33×10^7	0.5	22,500
5	3.90×10^{10}	−0.18	69,200	1.34×10^{11}	−0.43	0
6	2.33×10^6	0.5	65,710	4.60×10^9	−0.25	0

Table 3b Park multipliers for third body reactions

Species	M_1	M_2	M_3
CO_2	1	1	1
CO	1	1.95	1
O_2	1	1	1
C	1	14.8	5
O	1	14.8	5

where C_f, C_b, η_f, η_b, θ_f, and θ_b are constants. The values of these constants are supplied by either the McKenzie or the Park chemical kinetics model (see Tables 2 and 3). In addition to differences in reaction rate coefficients, the Park model also differs from the McKenzie model by the addition of a multiplier term, the purpose of which is to account for the efficiency of third body collisions. The appropriate reaction rate coefficient is multiplied by this factor.

A comparison of McKenzie and Park forward reaction rate coefficients for the dissociation of CO_2 is presented in Fig. 1. For $T<5000$ K, McKenzie predicts a faster reaction rate than Park. The discrepancy is as much as an order of magnitude for $T<2500$ K. However, for $T>5000$ K, Park predicts reaction rates faster than those of McKenzie. Figure 2 shows the comparison for the dissociation of CO. The two models predict similar rates and trends for the entire temperature range, with the Park rates only slightly lower. The forward reaction rate coefficients for the dissociation of O_2 are shown in Fig. 3. Once again the two models predict similar rates and trends. However, for this reaction Park predicts higher rates. For this study the driving reaction is the dissociation of CO_2. In addition, the majority of the flow is in the 5000–7000 K range. For this reason, Park predicts an overall faster reaction rate for the cases being studied.

Solution Procedure

The flowfield can be described as the solution of the Euler equations expanded to account for multiple reacting species and nonequilibrium vibrational energy. This set of coupled

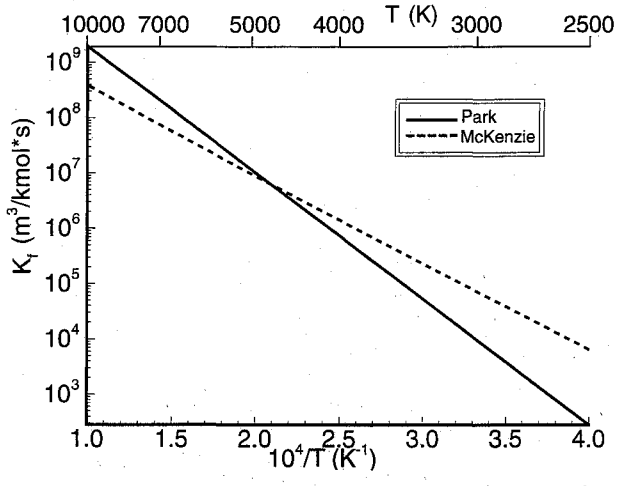

Fig. 1 Comparison of the forward reaction rates of McKenzie[1] and Park[4] for the dissociation of CO_2.

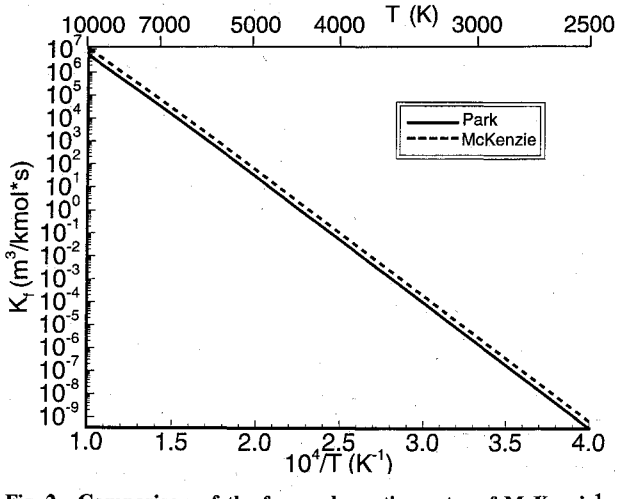

Fig. 2 Comparison of the forward reaction rates of McKenzie[1] and Park[4] for the dissociation of CO.

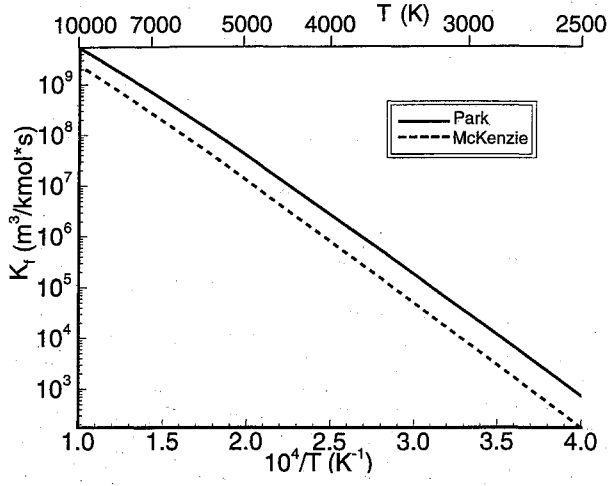

Fig. 3 Comparison of the forward reaction rates of McKenzie[1] and Park[4] for the dissociation of O_2.

partial differential equations is approximated in three dimensions using a finite volume, flux-vector splitting method developed by Candler[12] and Candler and MacCormack.[13] The approximate equations are solved using a lower-upper symmetric Gauss Seidel method[14–16] that has been modified to allow for the efficient treatment of thermochemical nonequilibrium flows.[17] The solution provides values of the thermodynamic variables throughout the flow. The converged solution is then used in conjunction with the multidimensional self adaptive grid (SAGE) code[18] to produce a flow adapted grid. The adapted grid is then used to produce a highly resolved flow solution for use in the computation of interferograms.

Computation of Interferograms

A Mach-Zehnder interferometer is an optical device that makes possible the visualization of density fields in a flow. The interferometer is sensitive to variations in the optical path length of a light beam passing through the flow. The optical path length is a function of the density and index of refraction of the species present. When this light beam is recombined with a reference beam that passes outside of the test section, the two constructively and destructively combine to form an interference pattern. This pattern is manifest through a series of dark and light fringes.

The form of the relation describing the interference patterns has been developed in several references.[19–21] For a gas composed of multiple species the expression for the optical fringe shift relative to the freestream is given by

$$F = \int_{z_1}^{z_2} \left(\Delta\rho \sum_{i=1}^{n} \frac{K_i}{\lambda} \frac{\rho_i}{\rho} \right) \mathrm{d}z \tag{10}$$

where z is the optical path length, λ is the wavelength of the light source, ρ_i/ρ is the mass fraction of species i, K_i is the Gladstone-Dale constant of species i, n is the number of species, and $\Delta\rho$ is the density change relative to the freestream. The limits of integration, z_1 and z_2, represent the length along the optical path length where the index of refraction is varying. In three dimensions this length is dependent on the region of the flow that the light beam passes through. The quantity actually recorded on the interferogram is the intensity of the interference of the recombined beams. The intensity I is proportional to F by

$$I \sim \cos^2(\pi F) \tag{11}$$

The values of the Gladstone-Dale constant are listed in Table 4.

The integration of Eq. (10) is performed along the optical path length of the light source passing through the flow. This

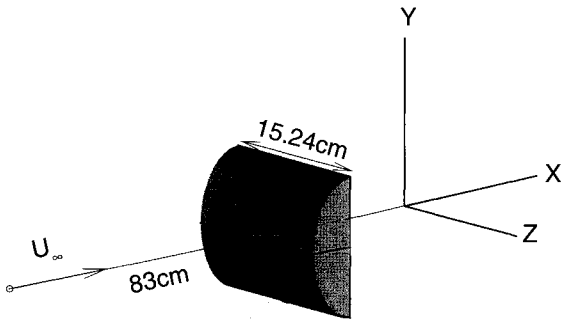

Fig. 4 Schematic of experimental model used in T3 free-piston shock tunnel.

path direction coincides with the z direction of the body-centered Cartesian coordinate system in Fig. 4. Since the flow solution is obtained on a curvilinear coordinate system, a line-of-sight calculation must be performed to evaluate the integral. This calculation is achieved by transforming the physical space into a computational space $(x, y, z) \rightarrow (\xi, \eta, \zeta)$. The ξ, η, and ζ directions correspond to the streamwise, body normal, and spanwise directions, respectively. The line-of-sight calculation can then be performed in the computational space in an efficient manner. The equation that governs this calculation is a function of the integration step dz and the mesh metrics x_ξ, x_η, y_ξ, y_η, z_ξ, and z_η. The equation is not a function of the ζ metrics because the calculation is performed in the ξ, η plane. The line-of-sight calculation requires that x and y remain constant ($dx = 0$ and $dy = 0$), whereas z (dz) is allowed to vary. Actually, the problem is overspecified. The lengths x and y form the legs of a right triangle with a hypotenuse of fixed length. Therefore, $dx = 0$ implies $dy = 0$ and vice versa and so $dx = 0$ or $dy = 0$ is sufficient. These two conditions lead to the following set of equations that govern the integral calculation:

$$d\xi = \frac{+x_\eta}{J}\,dz \qquad \text{and} \qquad d\eta = \frac{-x_\xi}{J}\,dz \tag{12a}$$

or

$$d\xi = \frac{+y_\eta}{J}\,dz \qquad \text{and} \qquad d\eta = \frac{-y_\xi}{J}\,dz \tag{12b}$$

where $J = z_\xi x_\eta - z_\eta x_\xi$ or $J = z_\xi y_\eta - z_\eta y_\xi$, respectively. A numerical approximation to the integral is performed by setting dz equal to a finite length Δz and marching along the optical path length in physical space for a fixed number of points in the xy plane. Equation (12) provides the corresponding $\Delta\xi$ and $\Delta\eta$ for the marching step in the computational space. The value of the fringe shift for each line of sight in the xy plane is then given by

$$F = \sum_{z_1}^{z_2} \left(\overline{\Delta\rho} \sum_{i=1}^{n} \frac{K_i}{\lambda}\,\overline{\rho_i} \right) \Delta z \tag{13}$$

The quantities in Eq. (13) are the same as those in Eq. (10) except that the overbar indicates that the variables have been averaged over the integration step.

Equation (13) shows the dependence of the fringe pattern on density and mass fractions. At each point in the flow, these values are dependent on the chemical kinetics and vibrational energy models. Therefore, changes in the CO_2 thermophysical model are observed in the interferograms and may be directly compared to experimental data.

Experimental Data

A series of circular and elliptical cylinders of varying radii and eccentricities was tested. The geometries of these cases are listed in Table 5. All of the cylinders have a length of 15.24 cm

Table 4 Gladstone-Dale constants for use in Eq. (10) with values from Refs. 20–22

Species	K, 10^3 m^3/kg
CO_2	0.230
CO	0.270
O_2	0.190
C	0.404
O	0.182

Table 5 Semimajor and semiminor axes for elliptical geometries and wavelength of interferogram for dissociating CO_2

Case	$a:b$	a, cm	b, cm	λ, nm
1	3:2	6.35	4.23	533
2	3:1	2.54	0.846	533
3	1:1	2.54	2.54	433
4	1:1	5.08	5.08	433
5	2:1	3.81	1.91	533

and are located in a conical flow with a point source 83.0 cm upstream of the leading edge of the model. A schematic of the experiment is shown in Fig. 4. The nominal freestream conditions are $u_\infty = 4.24$ km/s, $\rho_\infty = 7.27 \times 10^{-3}$ kg/m^3, and $T_\infty = 1970$ K, with mass fractions of $c_{CO_2\infty} = 0.268$, $c_{CO\infty} = 0.445$, $c_{O_2\infty} = 0.155$, $c_{O\infty} = 0.133$, and a trace of gaseous carbon. These freestream mass fractions were computed assuming freezing near the nozzle throat. There is some uncertainty in these values, but errors of 10% were found not to affect the results.

These freestream conditions lead to a Mach number on the order of 5. This Mach number is lower than Mach numbers of typical entry conditions. However, an analysis of steady-state, dissociation-dominated flows reveals that the similarity parameters are

$$\left(\frac{r\rho_\infty}{u_\infty}\right)_{\text{exp}} = \left(\frac{r\rho_\infty}{u_\infty}\right)_{\text{flight}} \qquad (h_{0\infty})_{\text{exp}} = (h_{0\infty})_{\text{flight}} \tag{14}$$

where r is a characteristic length, which was taken to be the nose radius. The terms ρ_∞, u_∞, and $h_{0\infty}$ are the freestream density, velocity, and total enthalpy, respectively. This result comes from the binary scaling that governs dissociating flows.[23]

The similarity parameters for the experiment performed by Hornung are calculated to be $(r\rho_\infty/u_\infty)_{\text{exp}} = 3.71 \times 10^{-8}$ kg s/m^3 and $(h_{0\infty})_{\text{exp}} = 9.06$ MJ/kg. A comparison to the flight conditions being studied for the Martian environmental survey[6] (MESUR) aeroshell, $(r\rho_\infty/u_\infty)_{\text{MESUR}} = 4.36 \times 10^{-8}$ kg s/m^3 and $(h_{0\infty})_{\text{MESUR}} = 10.4$ MJ/kg, demonstrate that the experimental data are similar to the flight regimes to be encountered by this entry vehicle in the Martian atmosphere.

Results

Computational interferograms have been produced for five experimental cases using both the Park et al. and the McKenzie chemical kinetics models. The initial solutions were performed on $30 \times 50 \times 30$ computational grids. Figures 5 and 6 show the experimental comparison for case 1. The two models produce similar solutions, and it is only through a detailed comparison to the interferogram fringe patterns that the accuracy of each model can be assessed. The Park chemical kinetics model produces an interferogram in excellent agreement with the experiment, whereas the McKenzie model produces a less accurate result. The Park model slightly underpredicts the shock stand-off distance, but the computational stand-off distance would be increased slightly with the inclusion of the

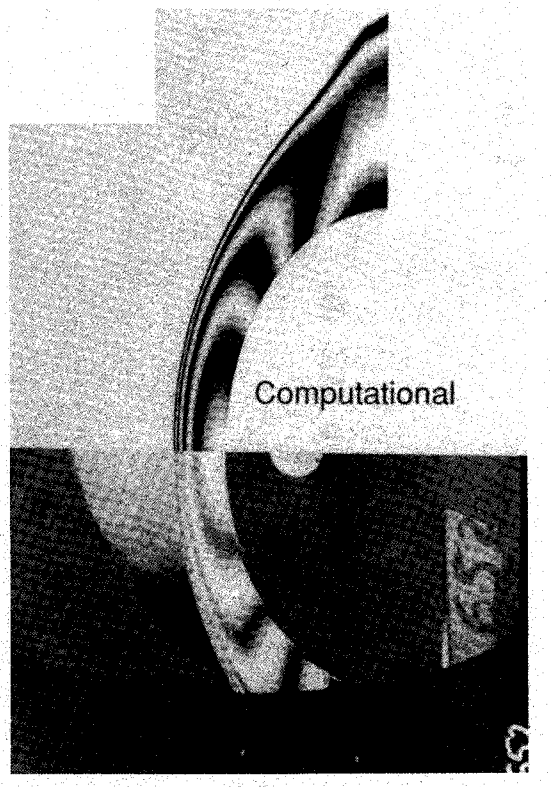

Fig. 5 Comparison of case 1 experimental and computational interferograms for the McKenzie[1] rate model on 30 × 50 × 30 grid.

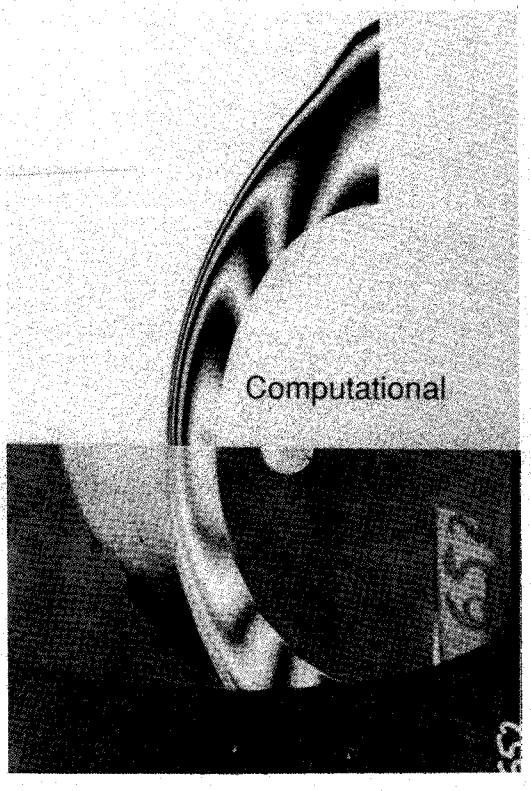

Fig. 6 Comparison of case 1 experimental and computational interferograms for the Park et al.[4] rate model on 30 × 50 × 30 grid.

boundary layer. The McKenzie model overpredicts the standoff distance; the comparison would be made worse if the viscous effects were included in the computation. A careful overlaying of the fringe patterns indicates that the Park model produces better agreement of the fringe locations and shapes. For example, the full fringe closest to the stagnation point is too thick in the McKenzie model simulation, whereas the thickness is very close in the Park model computation. Overall, the Park model produces excellent agreement with the details of the fringe patterns, except for the boundary layer that appears in the experimental interferogram. The overprediction of the shock-layer thickness in the McKenzie model simulations is due to an underprediction of density rise. This

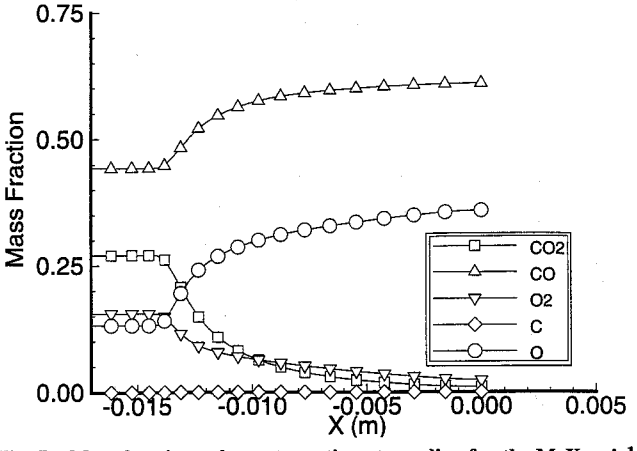

Fig. 7 Mass fractions along stagnation streamline for the McKenzie[1] rate model on 30 × 50 × 30 grid.

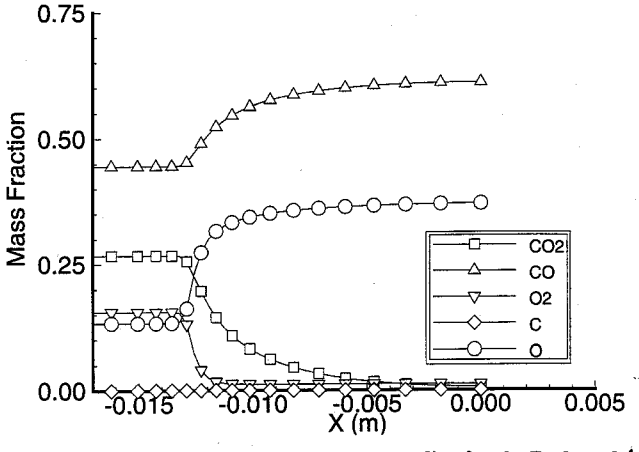

Fig. 8 Mass fractions along stagnation streamline for the Park et al.[4] rate model on 30 × 50 × 30 grid.

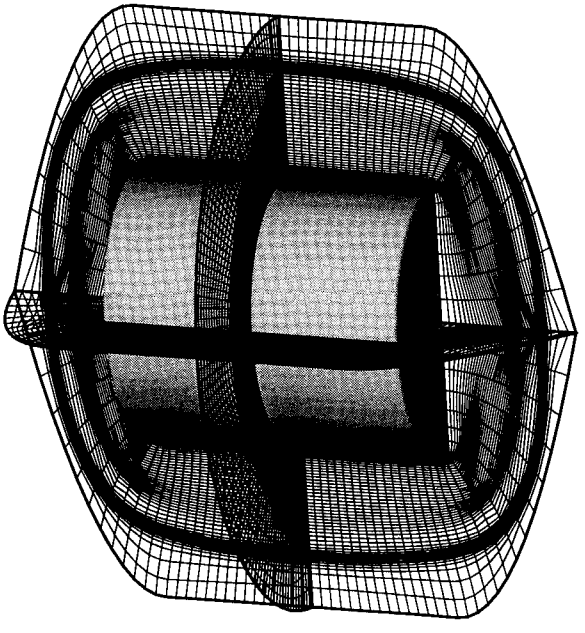

Fig. 9 50 × 50 × 30 adapted grid for case 1.

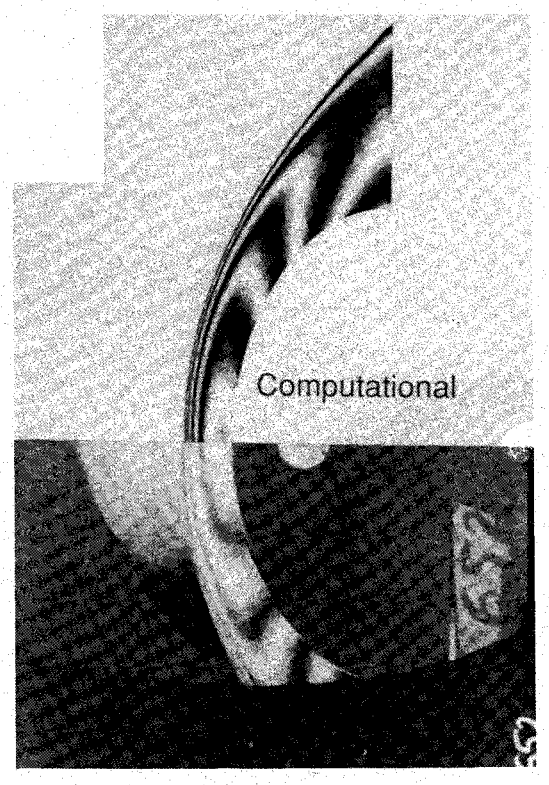

Fig. 10 Comparison of case 1 experimental and computational interferograms for the Park et al.[4] rate model on 50 × 50 × 30 grid.

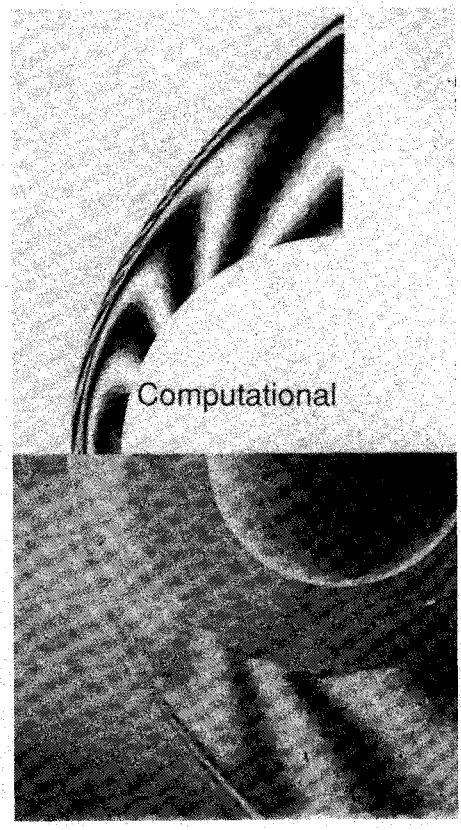

Fig. 12 Comparison of case 3 experimental and computational interferograms for the Park et al.[4] rate model on 50 × 50 × 30 grid.

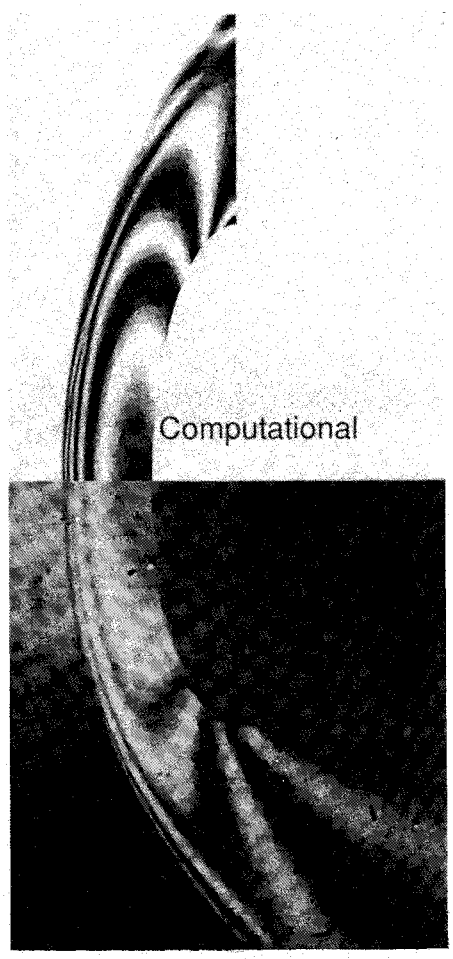

Fig. 11 Comparison of case 2 experimental and computational interferograms for the Park et al.[4] rate model on 50 × 50 × 30 grid.

effect is verified throughout the flowfield by an underprediction in the fringe shift. The McKenzie rates predict a maximum density rise of $(\rho/\rho_\infty)_{max} = 9.05$, slightly lower than the $(\rho/\rho_\infty)_{max} = 9.35$ predicted by the Park rates. However, this small discrepancy in the density rise results in a significant change in the computed interferograms.

The influence of the reaction rates on the density rise can be seen in the plots of the mass fractions along the stagnation line as seen in Figs. 7 and 8. The Park rates predict a faster dissociation of O_2. This faster rate is consistent with the rate comparison of Fig. 2. Park predicts only a moderate increase in the dissociation rate of CO_2 as compared to the McKenzie rate. This moderate difference is accounted for by the fact that both chemical kinetics models predict a temperature behind the shock of approximately 5000 K. Therefore, for a large portion of the shock layer the two models predict almost identical CO_2 dissociation rates as shown in Fig. 1. However, at the higher temperatures in the vicinity of the shock, Park predicts faster dissociation rates. As a result of the high temperatures near the shock and the faster dissociation rate of O_2, Park predicts overall faster reaction rates resulting in a greater density rise.

Cases 2–4 produced similar results, with the Park reaction rates very closely reproducing the experiment. The McKenzie reaction rates consistently underpredicted the density rise. The results of case 5 were inconclusive. For case 5, neither reaction rate model showed a close comparison to the experiment. Both models significantly overpredicted the density rise. Because of the close comparison and similar results of the first four cases, the conclusion is that the experimental data of case 5 differ significantly from the nominal test conditions. On the basis of the comparisons of the first four cases, the conclusion is that the Park et al. model more closely predicts the physics of the dissociation dominated flow for the temperature and energy range of the experiment. For this reason, the McKenzie model was abandoned and a more detailed analysis was performed on the Park et al. model.

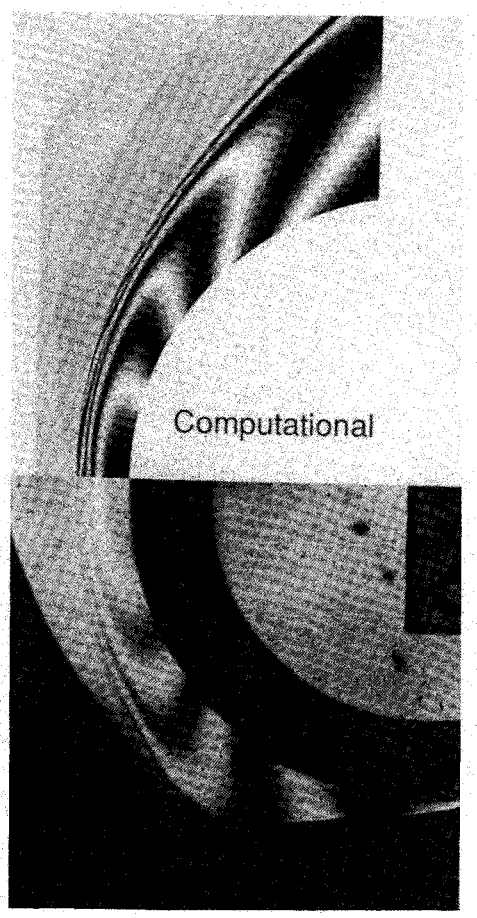

Fig. 13 Comparison of case 4 experimental and computational interferograms for the Park et al.[4] rate model on 50 × 50 × 30 grid.

Solutions were obtained for the Park et al. model on uniformly distributed 50 × 50 × 30 grids. The converged solutions were then used in conjunction with the SAGE code[18] to adapt the finite volume grids to regions with high density and mass fraction gradients. This ensures the most efficient use of the grid points in computing interferograms. Converged solutions were then obtained on the 50 × 50 × 30 adapted grids ensuring adequate resolution of the flow features. Figure 9 shows a representative adapted grid. Due to the symmetry of the flowfield, only one-quarter of the cylinder needs to be modeled. In Fig. 9 all four quadrants are shown for clarity.

Figures 10–13 show the experimental comparison for Park's reaction rate model on the dense grid for cases 1–4, respectively. All four cases show close comparison to the experimental data. The discrepancies that exist are minor and can be accounted for by the margin of error in the experimental data. The nozzle reservoir pressure has an uncertainty of ± 12%, and the shock velocity has an uncertainty of ± 5%. For this reason, the Park et al. chemical kinetics model has been validated as closely as possible for the available experimental data.

An investigation was also performed to study the effects of the modeling of the vibrational relaxation time on the experimental comparison. Both the Millikan-White expression using $\theta_v = 945$ K for all modes [Eq. (5)] and the Camac expression [Eq. (7)] were implemented on identical grids for case 1. The interferograms produced were insensitive to the relaxation model employed. No differences in the computed interferograms could be discerned. However, a plot of the temperature profiles along the stagnation line revealed differences in the two models (see Fig. 14). The Millikan-White expression predicted a slower relaxation time, resulting in increased thermal nonequilibrium. The differences in the temperature profiles are small compared to the differences produced by the choice

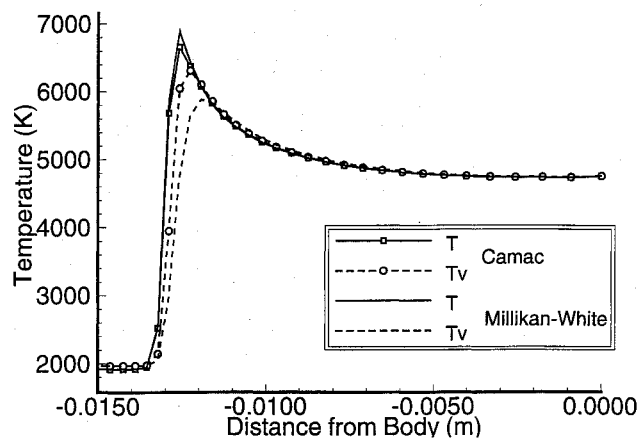

Fig. 14 Comparison of temperature distribution along stagnation line for Millikan-White and Camac vibrational relaxation expressions.

of the chemical kinetics model. Also, Chen et al.[6] showed that the effect of vibrational relaxation time on surface heating rates is negligible. Therefore, the chemical kinetics model employed is of greater importance. Because the Camac expression is a direct fit to experimental data for dissociating CO_2 flows, it should be used.

Conclusions

The results of this study demonstrate that, for the cases examined, the chemical kinetics model of Park et al. reproduces the available experimental data more accurately than the chemical kinetics model of McKenzie. The Park reaction rate model produces results in very good agreement with experiment. Within the limitations of the experiment and the sensitivity of the interferograms to density variations, it is not possible to offer any improvements to this chemical kinetics model. This model has been shown to correctly model the physics of the flow for conditions in the range $h_{0\infty} = 10$ MJ/kg and $2000 < T < 7000$ K. Further studies need to be performed to validate the model for flows with higher postshock temperatures. With this exception, the Park et al. model has been shown to correctly model the density field at conditions similar to Martian entry flows. It should be noted that the experimental freestream is partially dissociated, making a direct comparison to actual flight conditions difficult.

The comparison to experimental interferograms was shown to be insensitive to the vibrational relaxation model employed. This insensitivity is due in part to the very fast vibrational relaxation time of CO_2. However, the expression developed by Camac is a direct fit to experimental data for dissociating CO_2 flows. Therefore, the Camac expression is preferred to the Millikan-White expression for the relaxation time of CO_2. Further work needs to be performed to validate the premise that the vibrational energies of all of the species can be characterized by a single temperature T_v. The strong resonance coupling that exists between the vibrational modes of the CO_2 molecule may not extend to other molecules. In particular, a decoupling of the CO molecule may require the modeling of separate vibrational temperatures T_{vCO_2} and T_{vCO}. The investigation of these vibrational relaxation models will require new experiments that have been specifically designed to be sensitive to changes in vibrational energy.

Acknowledgments

This work was supported by the following grants: NASA Langley Research Center Cooperative Agreement NCC1-140 with the Aerothermodynamics Branch of the Space Systems Division, and NASA Grant NAGW-1331 to the Mars Mission Research Center at North Carolina State University.

References

[1]McKenzie, R. L., "An Estimate of the Chemical Kinetics Behind Normal Shockwaves in Mixtures of Carbon Dioxide and Nitrogen for Conditions Typical of Mars Entry," NASA TN D-3287, Feb. 1966.

[2]Evans, J. S., Schexnayder, C. J., Jr., and Grose, W. L., "Effects of Nonequilibrium Ablation Chemistry on Viking Radio Blackout," *Journal of Spacecraft and Rockets,* Vol. 11, No. 2, 1974, pp. 84–88.

[3]Grose, W. L., Falanga, R. A., and Sutton, K., "An Analysis of Communications Blackout for Pioneer Venus Entry Probes," AIAA Paper 75-182, Jan. 1975.

[4]Park, C., Jaffe, J., Howe, J., and Candler, G. V., "Chemical Kinetic Problems of Future NASA Missions," AIAA Paper 91-0464, Jan. 1991.

[5]Candler, G. V., "Computation of Thermo-Chemical Nonequilibrium Martian Atmospheric Entry Flows," AIAA Paper 90-1695, June 1990.

[6]Chen, Y. K., Henline, W. D., Stewart, D. A., and Candler, G. V., "Navier-Stokes Solutions with Surface Catalysis for Martian Atmospheric Entry," *Journal of Spacecraft and Rockets,* Vol. 30, No. 1, 1993, pp. 32–42; also AIAA Paper 92-2946, July 1992.

[7]Camac, M., "CO_2 Relaxation Processes in Shock Waves," *Fundamental Phenomena in Hypersonic Flow,* edited by J. G. Hall, Cornell Univ. Press, Ithaca, NY, 1966, pp. 195–215.

[8]Vincenti, W. G., and Kruger, C. H., Jr., *Introduction to Physical Gas Dynamics,* Krieger, Malabar, FL, 1965, pp. 198–206.

[9]Millikan, R. C., and White, D. R., "Systematics of Vibrational Relaxation," *Journal of Chemical Physics,* Vol. 39, No. 12, 1963, pp. 3209–3213.

[10]Gaydon, A. G., "Temperature Measurement and Relaxation Processes in Shock Tubes," *Fundamental Phenomena in Hypersonic Flow,* edited by J. G. Hall, Cornell Univ. Press, Ithaca, NY, 1966, pp. 159–170.

[11]Park, C., *Nonequilibrium Hypersonic Aerothermodynamics,* Wiley, New York, 1990, pp. 57–60.

[12]Candler, G. V., "The Computation of Weakly Ionized Hypersonic Flow in Thermo-Chemical Nonequilibrium," Ph.D. Thesis, Dept. of Aeronautics and Astronautics, Stanford Univ., Stanford, CA, June 1988.

[13]Candler, G. V., and MacCormack, R. W., "Computation of Weakly Ionized Hypersonic Flows in Thermochemical Nonequilibrium," *Journal of Thermophysics and Heat Transfer,* Vol. 5, No. 3, 1991, pp. 266–273.

[14]Yoon, S., and Jameson, A., "An LU-SSOR Scheme for the Euler and Navier-Stokes Equations," AIAA Paper 87-0600, Jan. 1987.

[15]Eberhardt, S., and Imlay, S. T., "A Diagonal Implicit Scheme for Computing Flows with Finite-Rate Chemistry," AIAA Paper 90-1577, June 1990.

[16]Imlay, S. T., Roberts, D. W., Soetrisno, M., and Eberhardt, S., "Nonequilibrium Thermo-Chemical Calculations using a Diagonal Implicit Scheme," AIAA Paper 91-0468, Jan. 1991.

[17]Hassan, B., Candler, G. V., and Olynick, D. R., "The Effect of Thermo-Chemical Nonequilibrium on the Aerodynamics of Aerobraking Vehicles," AIAA Paper 92-2877, July 1992.

[18]Davies, C. B., and Venkatapathy, E., "Application of a Solution Adaptive Grid Scheme, SAGE, to Complex Three-Dimensional Flows," AIAA Paper 91-1594, June 1991.

[19]Goldstein, R. J., *Fluid Mechanics Measurements,* Hemisphere, New York, 1983, pp. 397–413.

[20]Merzkirch, W., *Flow Visualization,* Academic, New York, 1974, pp. 102–116.

[21]Alpher, R. A., and White, D. R., "Optical Refractivity of High-Temperature Gases. I. Effects Resulting from Dissociation of Diatomic Gases," *Physics of Fluids,* Vol. 2, No. 2, 1959, pp. 153–161.

[22]Kaye, G. W. C., and Laby, T. H., *Tables of Physical and Chemical Constants and Some Mathematical Functions,* Longman, New York, 1986, pp. 99, 100.

[23]Anderson, J. D., Jr., *Hypersonic and High Temperature Gas Dynamics,* McGraw-Hill, New York, 1989, pp. 581, 582.